Supplementary Information for

Vortical Reflection and Spiraling Fermi Arcs with Weyl Metamaterials

Hua Cheng[1,2*], Wenlong Gao[1*†], Yangang Bi[1,3*], Wenwei Liu[2], Zhancheng Li[2], Qinghua Guo[1], Yang Yang[1], Oubo You[1], Jing Feng[3], Hongbo Sun[3,4], Jianguo Tian[2], Shuqi Chen[2†], Shuang Zhang[1†]

[1]School of Physics & Astronomy, University of Birmingham, Birmingham B15 2TT, UK.

[2]The Key Laboratory of Weak Light Nonlinear Photonics, Ministry of Education, School of Physics, TEDA Institute of Applied Physics, and Renewable Energy Conversion and Storage Center, Nankai University, Tianjin 300071, China.

[3]State Key Lab of Integrated Optoelectronics, College of Electronic Science and Engineering, Jilin University, Changchun 130012, China

[4]State Key Laboratory of Precision Measurement Technology & Instruments, Department of Precision Instrument, Tsinghua University, Beijing 100084, China

*These authors contributed equally to this work.

†Corresponding author. Email: bhamwxg334@gmail.com (W.G); schen@nankai.edu.cn (S.C.); s.zhang@bham.ac.uk (S.Z.)

Supplementary Text

1. <u>Reflection under loss</u>

We consider material dissipations by adding imaginary part to the permittivity of the dielectrics $\varepsilon_d = \varepsilon' + i\varepsilon''$. It is found the winding of the reflection phases is robust against loss (Fig. S1). On the other hand, the presence of loss causes non-uniform reflection amplitude at different azimuth angle of incidence, and eigen polarization

states become elliptical, as shown in figure. S5. Despite this, the long and short axis of the elliptical polarization states represent the same π phase according to the azimuthal angle.
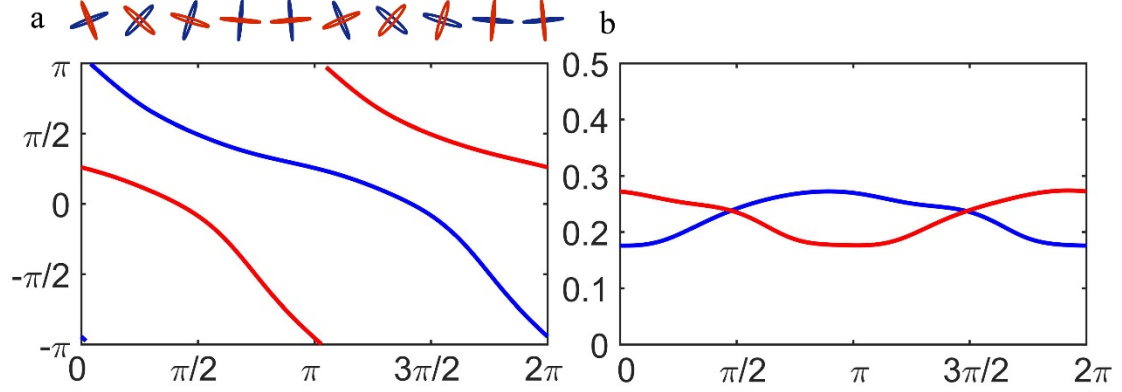
Fig. S1. Numerically simulated eigen-polarizations' reflection phase, reflection amplitude around the Weyl point under material loss. The loss is added to the hosting dielectrics of the metamaterial as the imaginary part of the relative permittivity$\varepsilon_d = \varepsilon' + i\varepsilon''$ where $\varepsilon'' = 0.1$.

2. <u>Derivation of equation (1)</u>

We start by deriving the expression of bulk eigen-fields of the metamaterial based on effective medium theorem. The Fermi arcs' eigen-fields can be decomposed into the bulk eigen-fields at momenta near the location of ideal Weyl points. For simplicity, we do not consider nonlocality in the metamaterial. Nonetheless, we found the distribution of reflection phase and the configuration of the spiraling fermi arcs can be well explained by the eigen-fields derived without considering the nonlocal effects. Maxwell equations, in Heaviside units, of the metamaterial can be written as:

$$n_x \begin{bmatrix} e_y \\ e_z \end{bmatrix} = \begin{bmatrix} \mu_y h_y \\ \mu_z h_z \end{bmatrix} - i\gamma \begin{bmatrix} e_y \\ e_z \end{bmatrix}$$

$$n_x \begin{bmatrix} h_y \\ h_z \end{bmatrix} = -\begin{bmatrix} \varepsilon_y e_y \\ \varepsilon_z e_z \end{bmatrix} - i\gamma \begin{bmatrix} h_y \\ h_z \end{bmatrix}$$

In the above equations, the coordinate is defined in Figure. 1 in the main text, e and h are electric and magnetic fields, respectively, n_x is the effective index along the x direction, and the $\varepsilon_{x,y,z}$, $\mu_{x,y,z}$ and γ are permittivity, permeability and the chirality,

describing the effective EM response of the metamaterial. The constraint imposed on the constitute relation is:

$$\varepsilon_{x,y}\mu_{x,y} - \gamma^2 = 0$$

which is subject to the longitudinal plasma mode resonance condition at the Weyl frequency.

With these conditions we can derive the ratios between the electromagnetic fields, and the effective index at the Weyl point n_x as:

$$\frac{e_y}{h_y} = \frac{\mu_z}{\mu_y}\frac{i\gamma}{\varepsilon_z}$$

$$\frac{e_z}{h_z} = i\sqrt{\frac{\mu_y}{\varepsilon_y}}$$

$$\frac{e_y}{e_z} = -i\mu_z\sqrt{\frac{\varepsilon_y}{\mu_y}}\frac{1}{n_x}$$

$$n_x = \sqrt{\varepsilon_y\mu_z + \varepsilon_z\mu_y}$$

Now we let $\eta_{y,z} = \sqrt{\frac{\mu_{y,z}}{\varepsilon_{y,z}}}$, and use the constitute relationship of single resonance chiral metamaterial in the y directions.

$$\varepsilon_y = \varepsilon_z - \frac{\omega_p{}^2}{\omega^2 - \omega_0{}^2}$$

$$\mu_y = \mu_z - \frac{F\omega^2}{\omega^2 - \omega_0{}^2}$$

$$\gamma = \frac{A\omega}{\omega^2 - \omega_0{}^2}$$

We have an identity $\sqrt{\varepsilon_z\mu_z} = \sqrt{\varepsilon_z\mu_y + \varepsilon_y\mu_z} = n_x$ at the Weyl frequency $\omega = \omega_p$. Note that ε_z and μ_z in the above expressions represent the non-resonant part of the dielectric constants because the resonance frequency of the Weyl metamaterial in the z direction is far above the Weyl frequency.

The non-normalized transverse eigen fields in the y-z directions can be simply written as:

$$|\varphi_t\rangle = \begin{bmatrix} 0 & 1 & i\eta_y/\eta_z & 0 & -i\eta_y/\eta_z{}^2 & 1/\eta_z \end{bmatrix}$$

The longitudinal field can be written as: $|\varphi_l\rangle = [\eta_y/\eta_z \quad 0 \quad 0 \quad -i/\eta_z \quad 0 \quad 0]$

Next our task is to decompose the eigen states in the metamaterial into the propagating eigen states in the ambient air. We note that the x components of the fields must be zero, otherwise the transversality condition of the fields in the ambient air would be violated.

Under normal incident approximation, which means $k_x \gg k_{y,z}$, at the Weyl frequency, Eigen states of the two Weyl points can be written as:

$$|W_1\rangle = e^{i\theta}|\varphi_t\rangle + |\varphi_l\rangle$$

$$|W_2\rangle = e^{i\theta}T|\varphi_l\rangle + T|\varphi_t\rangle$$

$$\theta = arctan(\frac{v_z k_z}{v_y k_y})$$

Where $T = [K, -K]$ is the time-reversal operator for photons, K is complex conjugate operator, $v_{y,z}$ are the Fermi velocities of the effective Weyl Hamiltonian in the y and z direction, which are almost identical in our metamaterial. Due to the vanishing of x component fields, the total field of the two Weyl points in the center can be expressed as:

$$|n_1\rangle = \begin{bmatrix} 0 & sin\,\theta & \dfrac{\eta_y}{\eta_z}cos\,\theta & 0 & -i\dfrac{\eta_y}{\eta_z^2}sin\,\theta & -i\dfrac{1}{\eta_z}cos\,\theta \end{bmatrix}$$

Similarly, for the other two Weyl points whose projections are located at large k's, we can write down the angle independent fields as:

$$|n_2\rangle = \begin{bmatrix} 0 & 0 & \dfrac{\eta_y}{\eta_z} & 0 & 0 & i\dfrac{\eta_y}{\eta_z^2} \end{bmatrix}$$

Now we define the plane wave modes' polarizations as linear polarization on either y or z:

The incident plane waves:

$$|In1\rangle = E_y^{i1}\begin{bmatrix} 0 & 0 & 1 & 0 & -\dfrac{1}{\eta_d} & 0 \end{bmatrix}$$

$$|In2\rangle = E_y^{i2}\begin{bmatrix} 0 & 1 & 0 & 0 & 0 & \dfrac{1}{\eta_d} \end{bmatrix}$$

The reflections:

$$|Re1\rangle = E_y^{r1}\begin{bmatrix} 0 & 0 & 1 & 0 & \dfrac{1}{\eta_d} & 0 \end{bmatrix}$$

$$|Re2\rangle = E_y^{r2}\begin{bmatrix} 0 & 1 & 0 & 0 & 0 & -\dfrac{1}{\eta_d} \end{bmatrix}$$

$E_y^{i1}, E_y^{i2}, E_y^{r1}$ and E_y^{r2} are complex number as weight of each mode in the scattering,

and we can define A and B as the weight of $|n_1\rangle$ and $|n_2\rangle$

Obeying the continuity of transverse electric and magnetic fields: $E_y^{i1}, E_y^{i2}, E_y^{r1}$ and E_y^{r2} can be expressed by A and B as:

$$E_y{}^{i1} = \frac{1}{2}[B\frac{\eta_y}{\eta_z} + A\frac{\eta_y}{\eta_z}\cos\theta + iA\frac{\eta_d\eta_y}{\eta_z{}^2}\sin\theta]$$

$$E_y{}^{r1} = \frac{1}{2}[B\frac{\eta_y}{\eta_z} + A\frac{\eta_y}{\eta_z}\cos\theta - iA\frac{\eta_d\eta_y}{\eta_z{}^2}\sin\theta]$$

$$E_y{}^{i2} = \frac{1}{2}[A\sin\theta - iA\frac{\eta_d}{\eta_z}\cos\theta + i\frac{\eta_d\eta_y}{\eta_z{}^2}B]$$

$$E_y{}^{r2} = \frac{1}{2}[A\sin\theta + iA\frac{\eta_d}{\eta_z}\cos\theta - i\frac{\eta_d\eta_y}{\eta_z{}^2}B]$$

These expressions allow us to get rid of A B, and express E_y^{r1} and E_y^{r2} with linear combinations of E_y^{i1} and E_y^{i2}, written in matrix form:

$$\begin{bmatrix} E_y^{r1} \\ E_y^{r2} \end{bmatrix} = \frac{1}{\sin\theta - i\frac{\eta_d}{\eta_z}\cos\theta - \frac{\eta_y\eta_d}{\eta_z{}^2}\left(i\cos\theta - \frac{\eta_d}{\eta_z}\sin\theta\right)}$$

$$* \begin{bmatrix} \sin\theta - i\frac{\eta_d}{\eta_z}\cos\theta - \frac{\eta_d\eta_y}{\eta_z{}^2}(i\cos\theta + \frac{\eta_d}{\eta_z}\sin\theta) & -2i\frac{\eta_d\eta_y}{\eta_z{}^2}\sin\theta \\ -2i\frac{\eta_d}{\eta_z}\sin\theta & \sin\theta\, i\frac{\eta_d}{\eta_z}\cos\theta + \frac{\eta_d\eta_y}{\eta_z{}^2}(i\cos\theta - \frac{\eta_d}{\eta_z}\sin\theta) \end{bmatrix} \begin{bmatrix} E_y^{i1} \\ E_y^{i2} \end{bmatrix}$$

This is the general expression of the scattering matrix around the Weyl point whose phase term of its eigen value is the equation (1) in the main text:

$$\phi_1(\theta) = \phi_2(\theta + \pi) = -i\ln\frac{(\frac{\eta_z}{\eta_d} - \frac{\eta_y\eta_d}{\eta_z{}^2})\sin\theta \pm i\sqrt{(1-\frac{\eta_y}{\eta_z})^2\cos^2\theta + 4\frac{\eta_y}{\eta_z}}}{(\frac{\eta_z}{\eta_d} + \frac{\eta_y\eta_d}{\eta_z{}^2})\sin\theta - i(1+\frac{\eta_y}{\eta_z})\cos\theta}$$

While this expression yields no concise analytical solutions for its eigenvalue and eigenvector a simplification assuming $\eta_z = \eta_y$, meaning the Weyl frequency is far from the resonance frequency, could give great simplifications. Note that $\eta_z = \eta_y$ might not be valid for the realistic Weyl metamaterial design, we still find excellent agreement between the numerical simulations and the fitted analytical expression. The scattering matrix then reads: $S = \frac{(1-\frac{\eta_d{}^2}{\eta_z{}^2})\sin\theta}{(1+\frac{\eta_d{}^2}{\eta_z{}^2})\sin\theta - i2\frac{\eta_d}{\eta_z}\cos\theta}\begin{bmatrix} 1 & 0 \\ 0 & 1 \end{bmatrix} +$

$\frac{2i\frac{\eta_d}{\eta_z}}{(1+\frac{\eta_d{}^2}{\eta_z{}^2})\sin\theta - i2\frac{\eta_d}{\eta_z}\cos\theta}\begin{bmatrix} -\cos\theta & -\sin\theta \\ -\sin\theta & \cos\theta \end{bmatrix}$, whose eigen values are:

$$\lambda^+ = \frac{(1 + i\frac{\eta_d}{\eta_z}\cot\frac{\theta}{2})}{(1 - i\frac{\eta_d}{\eta_z}\cot\frac{\theta}{2})}$$

and

$$\lambda^- = \frac{(1 - i\frac{\eta_d}{\eta_z} tan\frac{\theta}{2})}{(1 + i\frac{\eta_d}{\eta_z} tan\frac{\theta}{2})}$$

In the ideal case assuming impedance matching, $\eta_z = \eta_y = \eta_d = 1$, the first part of the scattering matrix S is demolished and can be simplified to equation (2) in the main text as:

$$\hat{S} = e^{-i\theta} \begin{bmatrix} cos\,\theta & sin\,\theta \\ sin\,\theta & -cos\,\theta \end{bmatrix}$$

To fit the numerical and the experimental data to equation (1) in the main text, note that $\eta_z = \sqrt{\frac{1}{\varepsilon_z}} = 0.6742$ and two extra parameters, a deviation in azimuthal angle ζ and an extra phase shift ξ need to be incorporated to fit equation (1) due to the nonlocal effects, which gives: $\phi_1' = \phi_1(\theta + \zeta) + \xi$, $\phi_2' = \phi_1'(\theta + \pi)$. As is shown in the Supplementary Figure S2, in small incident angle (4° 6°and 10°), the analytical result gives excellent agreement to the numerical results. The fitted η_y is around 0.97.
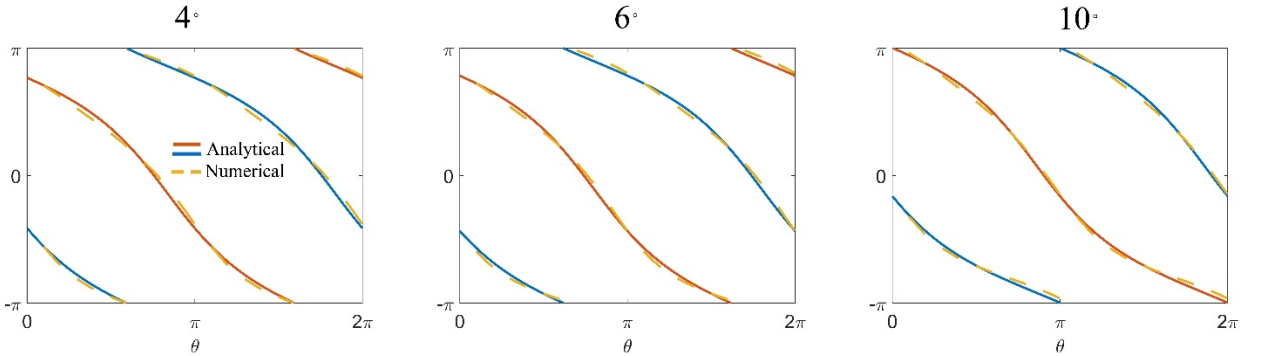
Fig. S2. Analytical and numerical reflection phases around the Weyl point at small angles. The fitting parameters are: 4°: $\eta_y = 0.9697$, $\zeta = 0.5077$ and $\xi = 0.4433$; 6°: $\eta_y = 0.9747$, $\zeta = 0.6347$ and $\xi = 0.3173$; 10° : $\eta_y = 0.9899$, $\zeta = 0.4443$ and $\xi = -0.2539.$,

In Figure 2B, however, due to the large incident angle 45° used in experiments since the horn antennas' large k range, η_y deviate from the small angle values. In this case, $\eta_y = 1.2323$, $\zeta = 0.4760$ and $\xi = -1.0472$. Note that even though the 45° incident angle doesn't satisfy the paraxial limit assumed in the theory, the topological

feature in the windings of reflection phases remains valid due to the topology of Weyl points.

3. <u>Analytical expression of the beam reflected by momentum space vortical mirror.</u>

Consider a Gaussian beam $|\varphi(v_r, \theta, x = 0)\rangle = \exp\left(-\frac{v_r^2}{4a}\right)|R\rangle$ incident onto the metamaterial, upon reflection $(\hat{S})$, it would be transformed into $|\varphi'(v_r, \theta, x = 0)\rangle = e^{-i2\theta}\exp\left(-\frac{v_r^2}{4a}\right)|L\rangle$, in which v_r is the radial direction Fourier component, $2\sqrt{a}$ is the 1/e position in the momentum space and $1/\sqrt{a}$ is the beam waist in real space. Under cylindrical Fourier transformation, $|\varphi'(v_r, \theta)\rangle$ in the real space reads $|\Phi'(r, \Theta, x = 0)\rangle = \left\{\int_0^\infty dv_r \cdot v_r exp(-\frac{v_r^2}{4a})J_2(v_r r)\right\}\exp(-i2\Theta)$, where J_n is the Bessel function of the first kind, r and Θ are the radial and polar angle of the polar coordinate in the real space on the surface of the Weyl metamaterial. The integration in the curly bracket is evaluated numerically and is illustrated in Fig. 2E. The phase profile is a 4π winding (Fig. 2F) and is consistent with the momentum space phase winding, and the total projected Chern number of Weyl points. The reflected beam under arbitrary projected Chern number n is given by

$$|\Phi'_n(r, \Theta, x = 0)\rangle = \left\{\int_0^\infty dv_r \cdot v_r exp(-\frac{v_r^2}{4a})J_n(v_r r)\right\}\exp(-in\Theta) \quad (S1)$$

The results for various integer n are provided in Fig. S3.
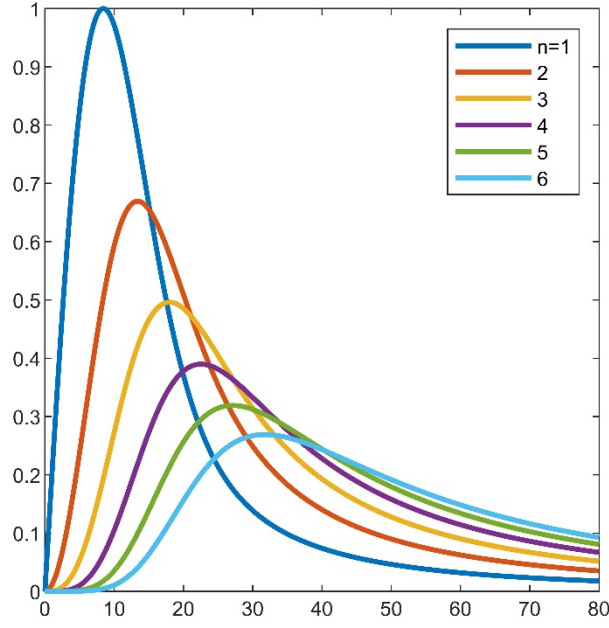
Fig. S3. Evaluated beam intensity profile according to equation (S1) for different integer n.

4. Scattering matrix for elliptical polarizations

The reflection matrix S in equation (2), main text, can be generalized to elliptical polarizations.

First, we suppose the scattering matrix operated on a elliptical polarization follows:

$$\hat{S}(\theta)\begin{bmatrix} a \\ ib \end{bmatrix} = e^{-in\theta}\begin{bmatrix} a \\ -ib \end{bmatrix}$$

According to the decomposition law of unitary matrices, the above equation can be transformed as:

$$\begin{bmatrix} \cos\theta & \sin\theta \\ -\sin\theta & \cos\theta \end{bmatrix}\begin{bmatrix} e^{i\alpha(\theta)} & 0 \\ 0 & e^{i\beta(\theta)} \end{bmatrix}\begin{bmatrix} \cos\theta & -\sin\theta \\ \sin\theta & \cos\theta \end{bmatrix}\begin{bmatrix} a \\ ib \end{bmatrix} = e^{-in\theta}\begin{bmatrix} a \\ -ib \end{bmatrix}$$

Which finally leads to the relations:

$$e^{i(\alpha(\theta)-\beta(\theta))} = \frac{-\sin\dfrac{\theta}{2}+iab\cos\dfrac{\theta}{2}}{-\sin\dfrac{\theta}{2}-iab\cos\dfrac{\theta}{2}}$$

5. Polarizations of the topological Fermi arcs

In Fig. S4, We start by showing the Fermi arcs and polarizations of the 7 mm waveguide configuration at the Weyl frequency using the numerical reflection data obtained at 10° oblique incidents. For simplicity, the scattering matrices are assumed to only varies in the angular direction but not along the radial directions. The corresponding Fermi arcs and polarization states are shown below.
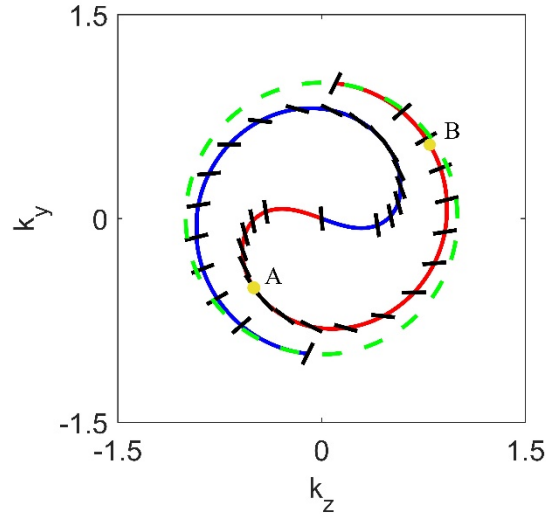
Fig. S4. Theoretical spiraling Fermi arcs and the polarizations

In the above figure, the Fermi arcs in the kz-ky plane are shown as solid blue and red spiraling lines, corresponding to the numerically solved reflection phases that can be fitted with $\phi_1(\theta)$ and $\phi_2(\theta)$ in Equation (1) in the main text. In-plane (z-y) electric field polarizations within the waveguide are obtained by numerically solving the eigen states of the corresponding scattering matrix, indicated by the solid black lines. Note that along the spiraling of the Fermi arcs, the polarization's direction rotates. Specifically, on the same spiraling Fermi arc, for example the red branch, polarization gradually varies from transverse electric (TE) on the A point to transverse magnetic (TM) on the B point. This behavior can be easily visualized in the impedance matching case whose eigen states are: $|\phi_1\rangle = \left[sin\frac{\theta}{2}; \ cos\frac{\theta}{2}\right]$ and $|\phi_2\rangle = \left[-cos\frac{\theta}{2}; \ sin\frac{\theta}{2}\right]$. The light cone in air is indicated by the dashed green circle where the spiraling is terminated. Similar behaviors are found in full wave simulated Weyl waveguide system as is shown

in the following picture,
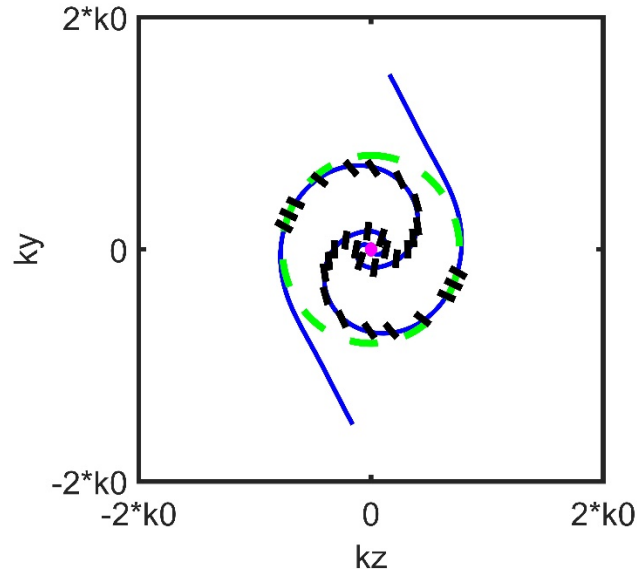
Fig. S5. Full wave simulated Fermi arcs and the polarizations.

Note that the detailed pattern of the spiral obtained by simulation is different from the theoretical results, due to the fact that: 1) finite Weyl metamaterial sample thickness utilized in the full wave simulation, causing deviations especially closer to the origin of the momentum space; 2) the scattering matrix could vary along radial direction due to higher order dispersions of the Hamiltonian that are neglected in the linear theory. However, the simple results have captured the main feature of the polarization state, i.e. the rotation of polarizations along the spiraling Fermi arcs. Note that the Fermi arcs, after joining the light cone, will gradually connect to the other two Weyl points of opposite-handedness outside of the light cone.

In the experiments, the excitation dipoles are fixed in the our-of-plane direction (x-axis). Therefore, Fermi arcs closer to the light cone away from the origin of the kz-ky plane are more preferentially excited due to the larger oblique angle of plane waves in the air, which is also observed in Supplementary Information Figure S8-S9. Combing the Ex, Ey and Ez results gives better visualization of the spiraling fermi arcs, however, there has been no general guidelines for the weight parameters, not only due to the complexity of polarization, but also the finite sample size, perturbations from the

detection dipole, & etc. Closer to the center, the fermi arcs could be further distorted due to the increase of the decay length of the surface mode and the finite thickness of the sample.

6. Measuring the surface states of the Weyl metamaterial

In the experiments, the vector network analyzer (VNA) was used to measure S parameters between the excitation and the probe dipole antenna. The Electric field is measured by inserting the probe dipole antenna deep into the waveguide from the side (as shown in Fig. 3c). The metallic wire connected to the probe antenna will interfere with the electric field in the waveguide. To minimize the influence of the metallic wire inside the waveguide, we measure the electric field within half y range, which is $[-az, az]\times[-ay, 0]$. Through centrosymmetric process, we augment the real space data to the whole range of $[-az, az]\times[-ay, ay]$. We probe the electric field of E_x, E_y, and E_z with the excitation direction in the x direction. The measured S parameter with the waveguide height of 7 mm at 13.5GHz is given in Fig. S6. The real space data of E_x, E_y, E_z are in (a-c) and the corresponding Fourier transformed data to momentum space (unit-less) are in (d-f).
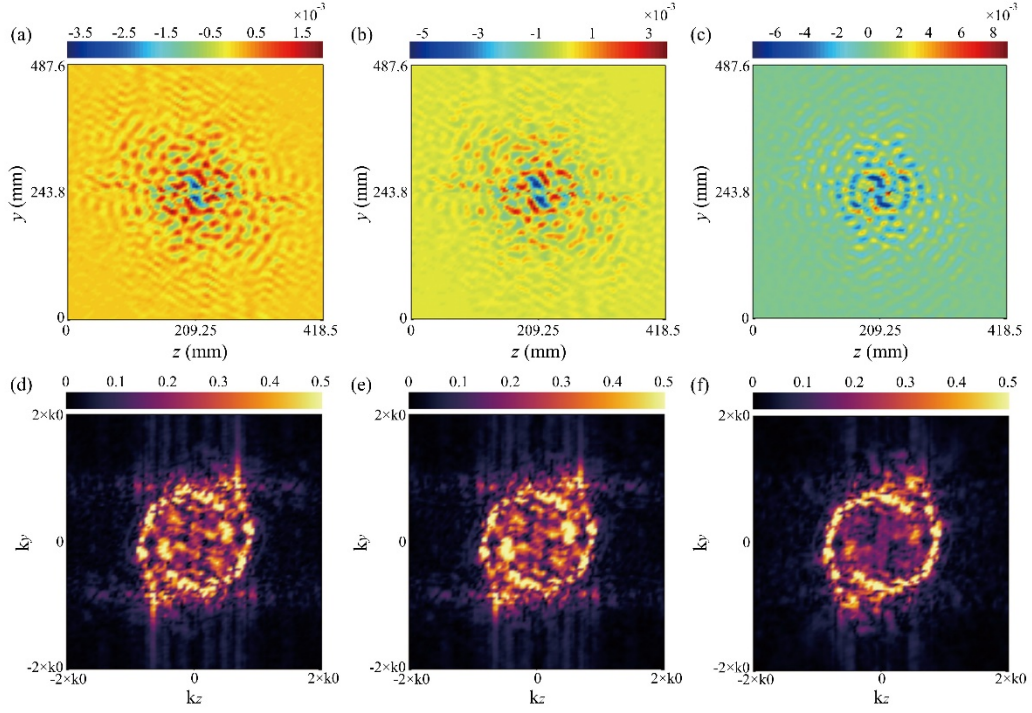
Fig. S6. **Experimental data of the near field measurement of Fermi arcs.** The real space data of Ex, Ey, Ez are in (a-c) and the corresponding Fourier transformed data to momentum space (unit-less) are in (d-f).

The measurement results shown in Fig. S7. A x-polarized electric dipole placed inside the sample close to the center of the top surface is used as the source, while another x-polarized electric dipole probe scans the top surface of the Weyl metamaterial to measure the E_x field component. The experimental results agree reasonably well with the simulation. The Fermi arcs connect between the light circle which contains two projected Weyl points overlapped at the center, and the other two projections of Weyl points outside the light circle with opposite chirality. The surface states inside the air circle leak into air rapidly and cannot propagate along the surface.
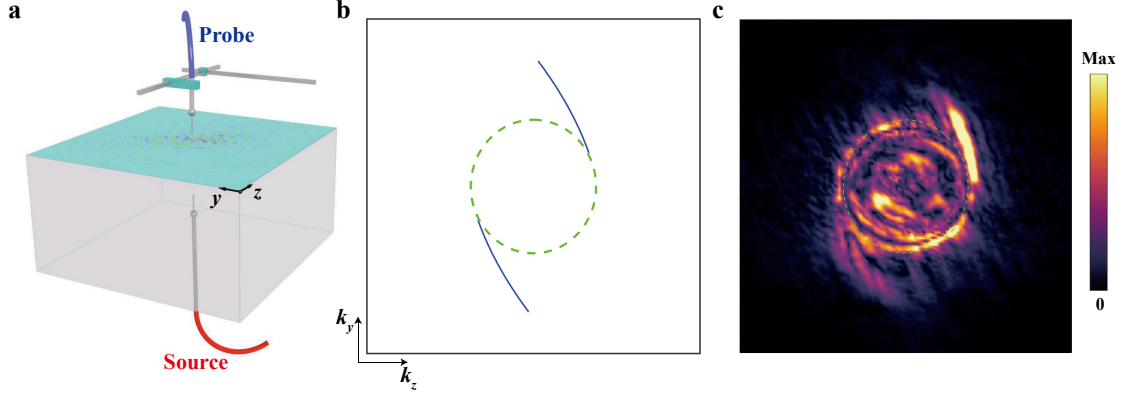
Fig. S7. Surface states of the Weyl metamaterial. (a) Near-field scanning system, where the source (red) is positioned in the center and near the top surface. (b) Simulated and (c) measured surface states at the frequency of 13.3 GHz. The green dashed circle indicates the air equi-frequency contour. The plotted range for the panels along k_z and k_y are $[-\pi/a_i, \pi/a_i]$, $i = z, y$ respectively.

7. Spiral Fermi arcs inside the waveguide.

The waveguide modes have inhomogeneous polarization configurations along the spiral Fermi arcs. To better visualize the spiral character of the Fermi arcs, all the field components of E_x, E_y, and E_z are measured and superposed linearly to get the total field.

Field components of different polarization provide complementary information for the observation of the spiral Fermi arcs. To obtain the complete picture of the Fermi arcs, we carry out a linear superposition of the field components. In all near field measurements, we set the scanning step as 4.5 mm (a_z) in z direction, and 3 mm (a_y) in y direction, which provide a surface momentum space range of $[-\pi/a_z, \pi/a_z] \times [-\pi/a_y, \pi/a_y]$ after the Fourier transformation.

To minimize the influence of the metallic wire of the probe antenna inside the waveguide, we only measure the electric field within half y range, which is $[-a_z, a_z] \times [-a_y, 0]$. Through centrosymmetric process, we obtain the electric filed in the whole range of $[-a_z, a_z] \times [-a_y, a_y]$. For the waveguide height of 7 mm, we get the total field by the linear superposition of $0.5 \times E_x + 0.5 \times E_y + E_z$, with results shown in Fig. S8. For the waveguide height of 11.5 mm, the linear superposition is $0.5 \times E_x + 0.1 \times E_y + E_z$, with results shown in Fig. S9. The spiral Fermi arcs for different waveguide heights are also

simulated in Fig. S10. As the height of waveguide increases, the spiral Fermi arc winds more. When the height of the waveguide approaches infinite, the spiral Fermi arc would wind infinitely and become extremely dense, which is equivalent to the bulk states of air.
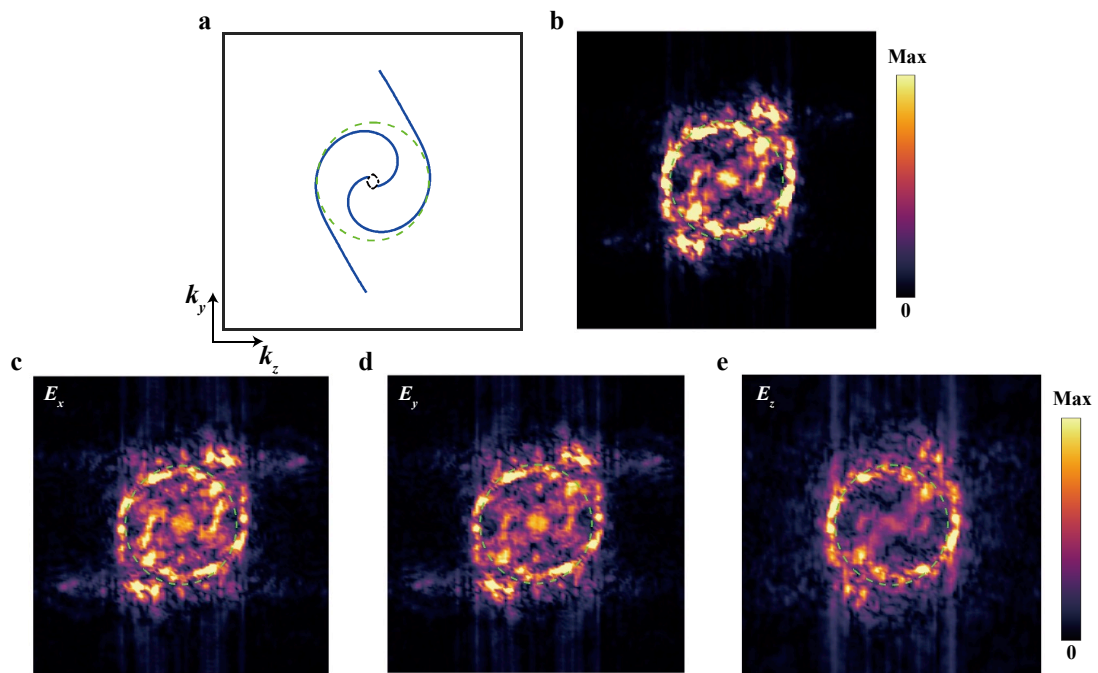
Fig. S8. Spiral Fermi arcs with waveguide height of 7 mm at frequency of 13.3 GHz. (a) The simulated spiral Fermi arc by Comsol Multiphysics. (b) The spiral Fermi arc which is superposed by the measured field components of (c) E_x, (d) E_y, and (e) E_z. The black dash-dotted circle denotes the bulk state and the green dashed circle denotes the air circle.
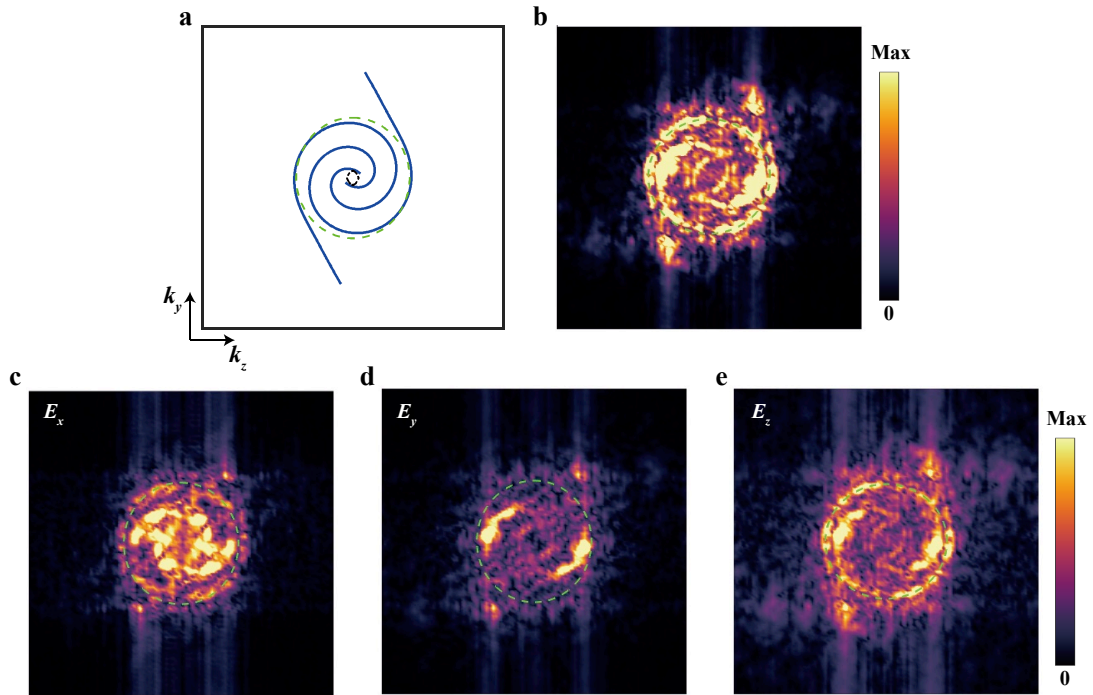
Fig. S9. Spiral Fermi arcs with waveguide height of 11.5 mm at frequency of 13.3 GHz. (a) The simulated spiral Fermi arc by Comsol Multiphysics. (b) The spiral Fermi arc which is superimposed by the measured field components of (c) E_x, (d) E_y, and (e) E_z. The black dash-dotted circle denotes the bulk state and the green dashed circle denotes the air circle.
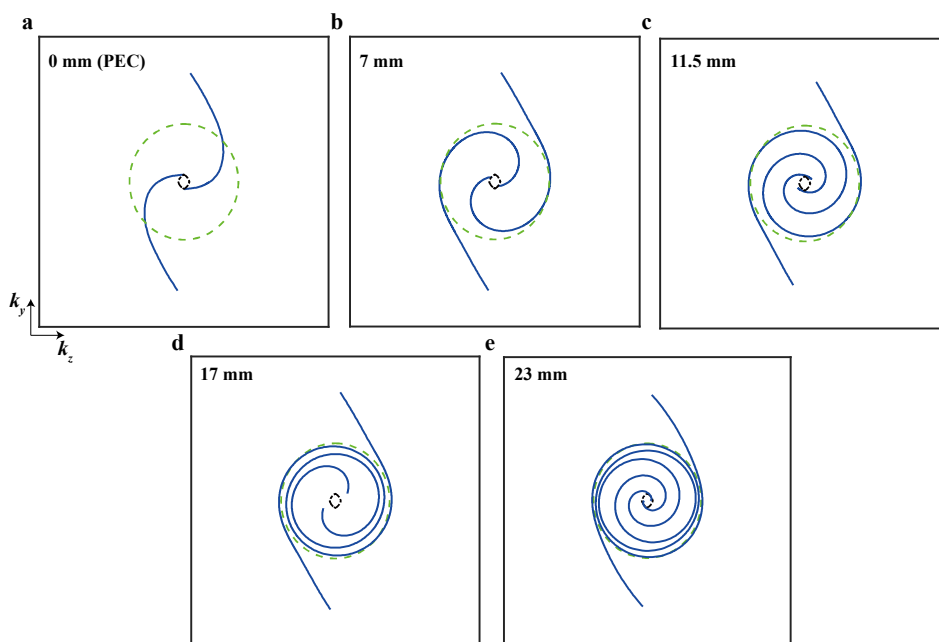
Fig. S10. Simulated spiral Fermi arc for different waveguide heights of (a) 0 mm, (b) 7 mm, (c) 11.5 mm, (d) 17 mm, and (e) 23 mm at the frequency of 13.3 GHz.

8. Experimental set up for measuring of reflection phases

For measuring the reflection phases, horn antennas are angled 45 degree to the y-z plane, the reflection amplitude and phases are collected by the Vector Network Analyzer (VNA) as is shown in Fig. S11. The Weyl metamaterial is rotated according to x axis for collecting reflections according to various azimuthal angle.
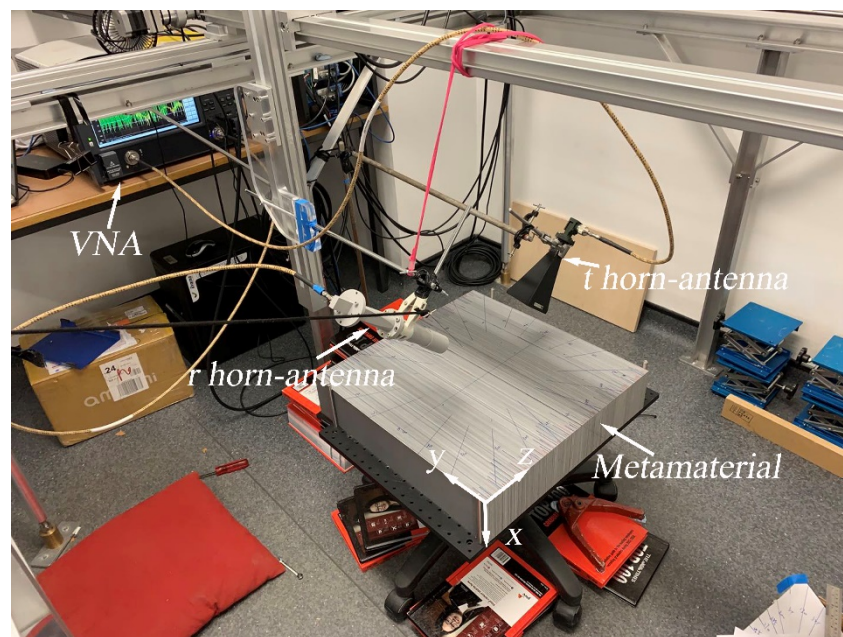
Fig. S11. Experimental set up for measuring of reflection phases